The Astrophysical Journal, 831:88 (7pp), 2016 November 1 doi:10.3847/0004-637X/831/1/88

SPITZER IRAC OBSERVATIONS OF IR EXCESS IN HOLMBERG IX X-1: A CIRCUMBINARY DISK OR A VARIABLE JET?

R. P. Dudik[1], C. T. Berghea[1], T. P. Roberts[2], F. Grisé[3], A. Singh[4], R. Pagano[5], and L. M. Winter[6]
[1] U.S. Naval Observatory (USNO), 3450 Massachusetts Avenue NW, Washington, DC 20392, USA; rachel.dudik@usno.navy.mil
[2] Centre for Extragalactic Astronomy, University of Durham, South Road, Durham DH1 3LE, UK
[3] Observatoire astronomique de Strasbourg, Université de Strasbourg, CNRS, UMR 7550, 11 rue de l'Université, F-67000 Strasbourg, France
[4] George Mason University, 4400 University Drive, Fairfax, VA 22030, USA
[5] St. John's College, 60 College Avenue, Annapolis, MD 21401, USA
[6] Atmospheric and Environmental Research, 131 Hartwell Avenue, Lexington, MA 02421, USA
Received 2016 April 19; revised 2016 August 12; accepted 2016 August 14; published 2016 October 28

ABSTRACT

We present *Spitzer* Infrared Array Camera photometric observations of the ultraluminous X-ray source (ULX, X-1) in Holmberg IX. We construct a spectral energy distribution (SED) for Holmberg IX X-1 based on published optical, UV, and X-ray data combined with the IR data from this analysis. We modeled the X-ray and optical data with disk and stellar models; however, we find a clear IR excess in the ULX SED that cannot be explained by fits or extrapolations of any of these models. Instead, further analysis suggests that the IR excess results from dust emission, possibly a circumbinary disk, or a variable jet.

Key words: black hole physics – galaxies: individual (Holmberg IX) – X-rays: binaries

1. INTRODUCTION

Ultraluminous X-ray sources (ULXs) are unusually bright X-ray sources, with $L_X > 10^{39}$ erg s^{-1}, which is approximately the Eddington limit for a $10\,M_\odot$ object (e.g., Feng & Soria 2011). Even though ULXs were discovered roughly 3 decades ago, the underlying mechanism that produces the powerful X-ray emission in many of these objects remains uncertain. However, after years of multiwavelength observations, only a few ULXs remain strong candidates for the intermediate-mass black hole (IMBH) scenario, such as HLX-1 in the galaxy ESO 243-49 (Farrell et al. 2009; Webb et al. 2012) and M82 X-1 (Strohmayer & Mushotzky 2003), while many others show indications of super-Eddington accretion and/or beaming from a stellar-mass black hole (e.g., Stobbart et al. 2006; Poutanen et al. 2007; Berghea et al. 2008; King 2008; Soria & Kuncic 2008; Gladstone et al. 2009; Liu et al. 2013; Sutton et al. 2013; Motch et al. 2014; Weng et al. 2014; Middleton et al. 2015) or a neutron star (Bachetti et al. 2014). Some galactic binaries are known to show super-Eddington luminosities, such as GRS 1915+105 (Fender & Belloni 2004) and V4641 Sgr (Revnivtsev et al. 2002), but not persistently as ULXs do. However, with the exception of a few distinct cases (see Liu et al. 2013; Middleton et al. 2013; Motch et al. 2014), conclusive evidence on the true nature of many ULXs remains unclear.

The ULX in Holmberg IX (Ho IX X-1 from now on) is one such enigmatic source. The ULX, also known as Holmberg IX X-1 or M81 X-9, has been well studied in the X-rays and optical since its discovery by the Einstein Observatory (Fabbiano 1988). In this paper we assume that the ULX is located at a distance of 3.6 Mpc (Gerke et al. 2011). Perhaps one of the most notable features of this ULX is the massive nebula in which it resides. Stretching 300 pc × 400 pc in size, the nebula was first discovered and associated with the ULX by Miller & Hodge (1994) and La Parola et al. (2001), respectively. The ultimate power source for the bubble nebula has been a matter of some debate. Some explanations for its origin include (1) the combined strength of multiple O stars and supernovae from the OB association in close proximity to the ULX, (2) a large hypernova event, or (3) winds and/or jets emanating from the ULX (e.g., Pakull & Mirioni 2002, 2003; Ramsey et al. 2006; Abolmasov et al. 2007; Abolmasov & Moiseev 2008; Pakull & Grisé 2008, p. 303).

The suggestion that winds or jets might power the massive nebular bubble around Ho IX X-1 is in line with the theory that many ULXs are similar to the famous supercritically accreting X-ray binary in our own Galaxy, SS 433, rather than an IMBH. Indeed, in the case of Ho IX X-1, the other two scenarios have ostensibly been ruled out as plausible explanations for the nebula distribution. For instance, Ramsey et al. (2006) showed that the energy released by six supernovae in the vicinity of the ULX is not sufficient to reproduce the energy of the expanding nebular shell, ruling out explanation 1 above. Pakull & Grisé (2008, p. 303) similarly find that the mechanical energy required to produce the nebula must result from a cluster that is more than two orders of magnitude larger than the observed stellar association. They also suggest that the period of time needed for mass transfer to begin in Ho IX X-1 is far shorter than required for a hypernova event to explain the birth of the ULX, ruling out explanation 2. Pakull & Grisé (2008, p. 303) suggest that winds and/or jets instead are more likely to power the bubble. Berghea et al. (2010a, Figure 10) support this finding, when they use shock models to describe the high-excitation optical lines seen in Ho IX X-1. Finally, Abolmasov et al. (2007) find radial velocity gradients that support the wind and/or jet explanation.

Many authors have noted the striking resemblance of Ho IX X-1 to SS 433. For instance, Fabrika et al. (2015) note that the optical spectrum of Ho IX X-1 is similar to wind-dominated objects like SS 433. In an X-ray study, Luangtip et al. (2016) see spectral variability patterns that are consistent with precession of the angle to the line of sight of the rotation axis of the ULX. This is very similar to what is seen in SS 433 as well. These scenarios hint that the processes powering emission in Ho IX X-1 and SS 433 may be similar, so much so that the two appear to be of the same family.

If the Ho IX X-1 nebula is indeed powered by jets, as is the case with its SS 433 "cousin," direct evidence of these jets has yet to surface. However, infrared photometry—an underused tool in the field of ULX astronomy—has the potential to produce a wealth of continuum information about the ULX that can be used to directly characterize the ULX SED. This has been done only once before for ULXs: in a study of Holmberg II X-1. In this study Berghea et al. (2010a, 2010b) used *Spitzer* mid-infrared data to constrain the ULX SED and found the data to be consistent with a broken power law typical of jet emission. The model was substantiated when Cseh et al. (2014) used the Karl G. Jansky Very Large Array (VLA) to image the ULX and found signatures of jets emanating from the ULX. On the other hand, infrared photometry has been widely used in the X-ray binary community to uncover excess from irradiated disks, circumbinary disks, and dusty shells from companions stars (Muno & Mauerhan 2006; Rahoui et al. 2010). Thus, *Spitzer* infrared photometry can be a powerful tool for uncovering structures and environments of ULXs that optical and X-ray data cannot.

In this paper we present *Spitzer* IRAC images of the ULX in Holmberg IX. Combining these images with multiwavelength optical, UV, and X-ray data from the literature, we model the Ho IX X-1 SED to determine the source of the infrared emission in this ULX. In Section 2 we provide the details of the *Spitzer* IRAC data analysis. In Section 3 we provide the fits to the full SED. In Section 4 we discuss the origin of the infrared emission. Finally, we summarize our results in Section 5.

2. INFRARED ARRAY CAMERA (IRAC) OBSERVATIONS AND DATA ANALYSIS

For this analysis, we used two sets of archival *Spitzer* IRAC data of the dwarf galaxy Holmberg IX taken on 2007 November 15 (Astronomical Observation Request, AORs 22537472 and 22537728). IRAC is a four-channel camera that provides 5.12×5.12 arcmin images at 3.6, 4.5, 5.8, and 8.0 μm. We processed the data both manually and using the post-processed basic calibrated data (PBCD) available for download from the archive, but found no difference between the two methods.

We used the *Spitzer* MOsaicker and Point Source Extractor (MOPEX) APEX package[7] to extract the photometric fluxes from the four channels. We followed the standard extraction procedure and conversion factors provided in the IRAC Instrument Handbook.[8] The pipeline mosaics for IRAC are accurate to within 20%[9] of the flux. All data calibration information, including background subtraction, are available in the footnoted links, as well as in Makovoz & Marleau (2005), which contains the exact point-source extraction procedure from MOPEX. To ensure that our IR data were extracted from the same region as the optical and X-ray data, we aligned the IRAC images with the *Hubble Space Telescope* (*HST*) Advance Camera for Surveys (ACS) F555W/V image using 11 common sources in both (*HST* ACS observation ID GO-9796 in Table 1). We find that the sources in the two images align to within $0\farcs11$ rms.

[7] http://irsa.ipac.caltech.edu/data/SPITZER/docs/dataanalysistools/tools/mopex/mopexusersguide

[8] http://irsa.ipac.caltech.edu/data/SPITZER/docs/irac/iracinstrumenthandbook/IRAC_Instrument_Handbook.pdf

[9] http://irsa.ipac.caltech.edu/data/SPITZER/docs/irac/iracinstrumenthandbook/74/

Table 1 provides fluxes extracted for the two sets of data, and Figure 1 shows false-color images of the ULX in 3.6, 4.5, and 8.0 μm compared with a standard *HST* ACS image of the ULX. We also used a SUBARU Hα image to overplot the contours of the bubble nebula. As the fluxes in Table 1 show, the observations at 5.8 and 8.0 μm show a weak detection in one case (AOR 22537472) and an upper limit in another (AOR 22537728) for a detection threshold of 4σ. Indeed, both observations are right on the line between detection and a nondetection for the 4σ threshold. Because the two sets of observations are identical in exposure time and because they are contiguous (i.e., one observation was taken right after the other), we chose to combine the two sets of observations to reduce the noise error on the measurements. The resultant fluxes are also provided in Table 1. The enhanced signal-to-noise ratio in the combined measurement suggests a statistically significant detection at 5.8 and 8.0 μm that can be used to characterize the IR emission.

3. SPECTRAL ENERGY DISTRIBUTION OF HOLMBERG IX X-1

To generate a full SED of Ho IX X-1, we used optical, UV, and X-ray data from the literature (Grisé et al. 2011; Berghea & Dudik 2012; Luangtip et al. 2016). A summary of all archival data used for this analysis is presented in Table 1. The optical data come primarily from *HST*, and the reduction strategy for these data can be found in Grisé et al. (2011). The UV data primarily come from the Optical Monitor on board *XMM-Newton*, and the data analysis strategy for these data can be found in Berghea & Dudik (2012). Finally, the X-ray data come from *XMM-Newton*, and the reduction strategy for these data can be found in Luangtip et al. (2016). We used the extinction $E(B-V) = 0.26$ adopted by Grisé et al. (2011) to correct for absorption in the UV, optical, and IR. The extinction curves used for this correction are taken from Cardelli et al. (1989).

This multiwavelength data sample spans 5 yr. We note that Ho IX X-1 is known to show X-ray variations of factors of 4–5 over days to years (Vierdayanti et al. 2010; Luangtip et al. 2016). Unfortunately, the only available multiwavelength data set that was taken of this object includes X-ray data from *Chandra* that suffer from severe pileup and are therefore unusable for the X-ray-fitting portion of this analysis (Grisé et al. 2011). However, we were able to use this *Chandra* data set to establish an estimate for the approximate X-ray flux during the same epoch as the *HST* data used here. Indeed, we find that the *Chandra* flux is very close to the mean between the two sets of *XMM* X-ray observations. Therefore, in the following, note that the actual *HST*-epoch X-ray flux is likely somewhere between the two *XMM* X-ray data sets and that the plotted data set provided here is *not* simultaneous. As the following sections will demonstrate, the multi-epoch nature of these data makes generating a good fit difficult.

X-ray spectra exist in the archives from *XMM-Newton*, *Swift*, and *NuSTAR*. Luangtip et al. (2016) found two main types of spectra: one hard ultraluminous (HUL)-like and one more disk-like (see also Sutton et al. 2013). We selected the *XMM-Newton* data sets 0112521101 and 0693851701 (referred to as obs 1 and obs 2, respectively, from here forward), which represent each of the two, typical ULX spectra regimes seen in this object.

Table 1
Multiwavelength Data

Instrument	Obs ID	Filter	Obs. Date	Flux Density (μJy)	Abs. (A_λ)	Corrected (μJy)
(1)	(2)	(3)	(4)	(5)	(6)	(7)
Spitzer IRAC	22537472	3.6	2007 Nov 15	4.99 ± 0.23	0.049	5.22 ± 0.24
Spitzer IRAC	22537472	4.5	2007 Nov 15	4.94 ± 0.36	0.046	5.15 ± 0.38
Spitzer IRAC	22537472	5.8	2007 Nov 15	6.98 ± 1.5	0.042	7.25 ± 1.57
Spitzer IRAC	22537472	8	2007 Nov 15	7.56 ± 1.8	0.039	7.65 ± 1.87
Spitzer IRAC	22537728	3.6	2007 Nov 15	4.89 ± 0.23	0.049	5.12 ± 0.24
Spitzer IRAC	22537728	4.5	2007 Nov 15	5.09 ± 0.36	0.046	5.31 ± 0.37
Spitzer IRAC	22537728	5.8	2007 Nov 15	<4.41	0.042	<4.59
Spitzer IRAC	22537728	8	2007 Nov 15	<5.45	0.039	<5.65
Combined IRAC	⋯	3.6	2007 Nov 15	4.94 ± 0.16	0.049	5.17 ± 0.17
Combined IRAC	⋯	4.5	2007 Nov 15	5.02 ± 0.25	0.046	5.23 ± 0.27
Combined IRAC	⋯	5.8	2007 Nov 15	5.70 ± 1.01	0.042	5.92 ± 1.10
Combined IRAC	⋯	8	2007 Nov 15	6.51 ± 1.28	0.039	6.75 ± 1.33
Hubble ACS	GO-9796	F814W/I	2004 Feb 7	2.99 ± 0.19	0.47	4.67 ± 0.29
Hubble ACS	GO-9796	F555W/V	2004 Feb 7	3.29 ± 0.15	0.81	7.06 ± 0.31
Hubble ACS	GO-9796	F435W/B	2004 Feb 7	3.87 ± 0.10	1.08	10.4 ± 0.29
Hubble ACS	GO-9796	F330W/U	2004 Feb 7	5.47 ± 0.23	1.33	18.6 ± 0.74
Hubble WFC3/IR	GO-12747	F160W/H	2012 Sep 25	1.01 ± 0.09	0.202	1.21 ± 0.12
XMM-Newton OM	0200980101	UVW1	2004 Sep 26	3.79 ± 0.32	1.51	15.2 ± 1.27
XMM-Newton OM	0200980101	UVM2	2004 Sep 26	<4.2	2.28	<34.2
XMM-Newton PN (obs. 1)	0112521001	0.3–10 keV	2002 Apr 10	⋯	⋯	⋯
XMM-Newton PN (obs. 2)	0693851701	0.3–10 keV	2012 Nov 12	⋯	⋯	⋯

Note. Columns: (1) Telescope and instrument name. (2) Observation ID. (3) Filter for the photometric observations and the wavelength range for the spectral observations; IRAC filters are microns. (4) Date of observation. (5) Flux density of photometric observations in μJy. (6) Total line-of-sight absorption for an extinction $E(B-V) = 0.26$. (7) Extinction-corrected photometric flux density in μJy.

3.1. Spectral Fitting

We used XSPEC version 12.7.1 to model the two X-ray spectra of Ho IX X-1 between 0.3 and 10 keV. The X-ray data were provided by and processed per the prescription of Luangtip et al. (2016). The X-ray data were fit with three models: multicolor disk (MCD) + comptonization model (compTT), self-irradiated funnel model (SIRF), and an irradiated disk model (DISKIR). Note that the former two were fit to the X-ray data only, while the latter (DISKIR) was fit to both the X-ray and optical data since that made the most physical sense for this model as described in the following.

We start with a model typically used to fit ULXs, with an accretion disk component (MCD in XSPEC) and the CompTT model to account for the Comptonization in a disk-corona geometry (e.g., Gladstone et al. 2009; Walton et al. 2014). We obtain good fits for both spectra. The parameter fit results are shown in Table 2.

The SIRF model (in XSPEC) describes the emission from a "supercritical funnel," similar to SS 433 (Abolmasov et al. 2009). The SIRF model provides acceptable fits for both sets of X-ray spectra. The accretion rate was fixed at 350× Eddington, the funnel opening angle was set to 30°, and the inclination angle was set to zero. The inner radius for this model is calculated in units of the "spherization radius" (Abolmasov et al. 2009). In order to better compare them with the other models, we convert them into units of km using the luminosity. We obtained estimates for the bolometric luminosities from the fitted X-ray models plus the jet model fit to the IRAC data (see Section 4). Then we used the accretion rate to estimate black hole masses of 41 and 107 $M_\odot$ for the first and second observations, respectively. The spherization radius can then be calculated (Abolmasov et al. 2009) for each black hole mass. Finally, we convert the fitted radii in the SIRF model to units of km. These are listed in column (5) in Table 2.

The DISKIR model is particularly useful when optical and UV data are available in addition to the X-ray spectrum. This is because many ULXs detected in the optical/UV show SEDs well fit by an irradiated disk (Berghea et al. 2010a; Berghea & Dudik 2012; Grisé et al. 2012). In this case it makes sense to fit the X-ray data together with the optical data, since the irradiation portion describes a large fraction of the optical/UV emission. Indeed, an irradiated disk was found to have an important contribution in the optical in other ULXs (e.g., Berghea & Dudik 2012). Following Gierlinski et al. (2008, 2009) and Berghea & Dudik (2012), we set the fraction of the flux thermalized in the inner disk at 0.1 and the radius of the Compton irradiated disk at 1.1 of the inner disk radius. A good fit requires that we set a large Comptonized luminosity ($\geqslant$ unilluminated disk luminosity) and an outer disk of radius 1000 $R_{\rm in}$ (where $R_{\rm in}$ is the inner disk radius), but this parameter is not well constrained. The fits are not acceptable statistically, but we obtained estimates for the irradiated flux fraction. It is large for both X-ray obs 2 (HUL-like, >6.8%) and X-ray obs 1 (disk-like, >5.7%). Typical values of 2%–4% have been found for previous fits of ULX X-ray/optical data sets with the DISKIR model (Berghea & Dudik 2012; Grisé et al. 2012; Tao et al. 2012).

Sutton et al. (2014) used an improved model for irratiated disks (one that accounts for the color–temperature correction) to fit a sample of ULXs with disk-like spectra. In this study, Sutton et al. (2014) compared the new DISKIR model results with a more traditional DISKIR model fit. They found that for most objects the reprocessing fraction is 10 times lower than predicted by traditional DISKIR models that do not include the color–temperature corrections, and that these new reprocessing

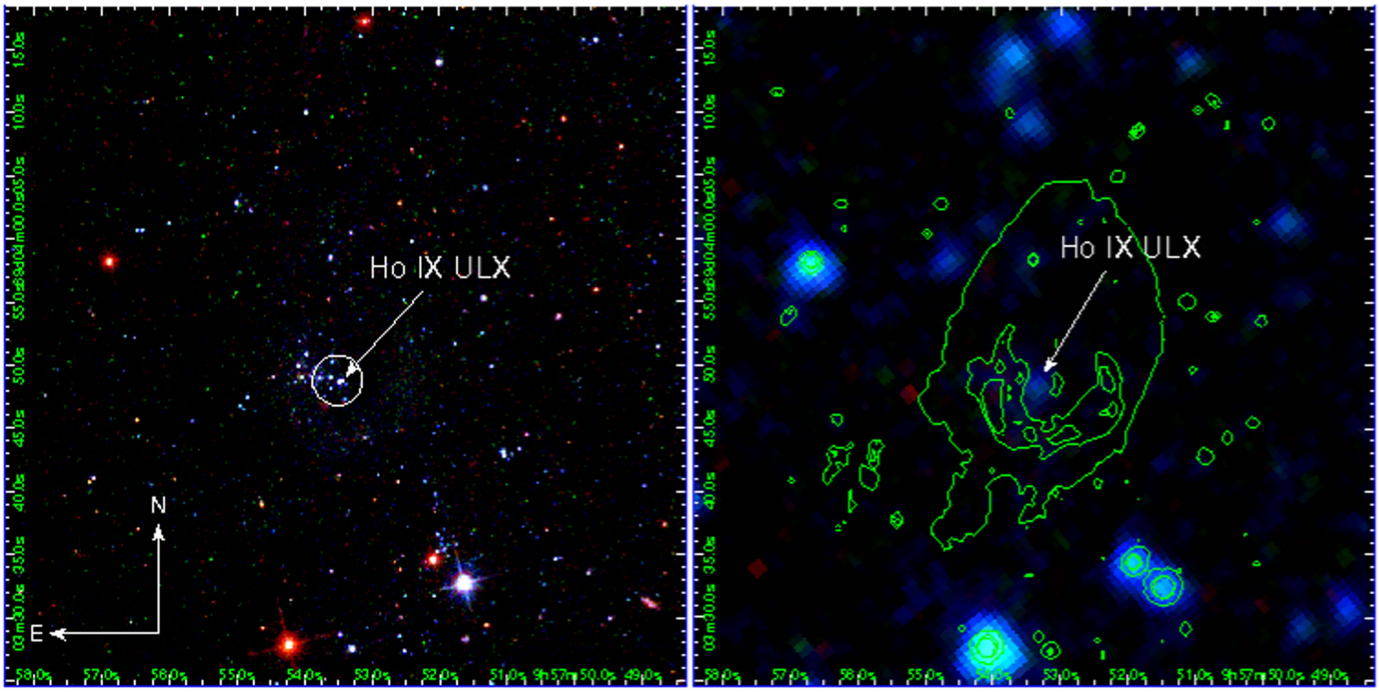

Figure 1. Left: *HST* ACS image in *R* (red), *V* (green), and *B* (blue) bands; right: IRAC image in 8.0 μm (red), 4.5 μm (green), and 3.6 μm (blue), with Hα contours from SUBARU FOCAS. The optical and IR counterpart is shown in both images, and the IRAC extraction aperture of 2″ radius is shown in the *HST* image.

fractions are closer to what is observed in Galactic binaries. However, for one of the brighter objects in that sample (NGC1313 X-2) they found a similar reprocessing fraction to ULXs where the spectrum may be more HUL-like. They interpreted the higher reprocessing fraction in the brighter ULX as originating in a higher scattering fraction onto the outer disk from the extensive wind thought to be driven off the disk; the high reprocessing fraction in Ho IX X-1 is consistent with this interpretation.

3.2. Extending the Models to Longer Wavelengths

In the following we construct the SED by extending the X-ray models we fit in the previous section to the optical/UV and IR data.

Extrapolated SIRF Model: The extrapolated SIRF models are plotted in Figure 2. Neither of these X-ray models fits the optical data well; however, the optical data are located between the two SIRF models. When the X-ray spectrum is disk-like, it overpredicts the optical data by a factor of 6.2. When the X-ray spectrum is HUL-like, it underpredicts the optical data by a factor of 3.2. Taking into account the variability of Ho IX X-1 and the multi-epoch nature of this data set, we conclude that a funnel model is capable of reproducing the optical and X-ray data. However, Figure 2 clearly shows that the SIRF model does not fit any of the IR data. Indeed, if this SIRF model were the appropriate model for the optical and X-ray data, an additional component would be needed to explain the IR excess.

Extrapolated Disk Models: As expected, simple disk models without irradiation are too faint in the optical. Our MCD +CompTT models shown in Figure 2 are more than an order of magnitude lower than the *HST* data if they are extrapolated into the optical. Following Grisé et al. (2011), we added a B0 Ib star to fit the optical photometry (black line in Figure 2) in this case, which resulted in a good fit to the data from X-ray to optical. The optical data are fit so well by the stellar model that an IR excess is clearly present at wavelengths longer than the *H*-band measurement. Thus, an additional component is needed to explain the IRAC data for the extrapolated disk model as well.

DISKIR model: Per Section 3.1 we began fitting the DISKIR data to the optical+X-ray data since it makes physical sense to do so when optical data are available. This extrapolated DISKIR model, described in Section 3.1, was a very good fit to the optical data but unfortunately not statistically acceptable overall for either X-ray data set. Here too, the DISKIR model is also not a good fit to the IRAC data.

Based on these fits and the multi-epoch nature of this data set, we conclude that all three models are plausible models for the optical/UV/X-ray data in Ho IX X-1. To definitively rule out any one model would require good, simultaneous optical and X-ray data (F. Grisé et al. 2016, in preparation). However, most importantly, none of these models fit the IR excess we see in Ho IX X-1, suggesting that another mechanism is responsible for this emission.

4. ORIGIN OF THE IR EMISSION IN HOLMBERG IX X-1

As Figure 2 shows, there is a clear IR excess in Ho IX X-1 that cannot be explained by the optical or X-ray models. The IR excess could be due to contamination from other stars within the 2″ extraction region; however, based on the B0 Ib stellar model in Figure 2 (which is also the brightest star in the 2″ extraction circle), we expect the contribution from all stars in that field to be negligible in the IR since their collective SEDs drop sharply at IR wavelengths.

There are four possible sources for the IR excess: (1) the irradiated disk/the companion star, (2) a heated dust shell, (3) a circumbinary disk such as those seen in X-ray binaries, or (4) a jet. Because none of the models from the previous sections produce sufficient emission in the IR to replicate our IRAC data, the latter three options are the only plausible emission

Table 2
Spectral Fits

Model	$N_{\rm H}$ (10^{21} cm^{-2})	$kT_{\rm in}$ (keV)	$\Gamma/\tau_{\rm e}$	$R_{\rm in}$ (10^3 km)	$kT_{\rm e}$ (keV)	χ^2_ν	log L (erg s^{-1})
(1)	(2)	(3)	(4)	(5)	(6)	(7)	(8)
X-ray + Optical							
DISKIR obs 1	2.3 ± 0.3	0.11 ± 0.02	1.82 ± 0.03	$90.2^{+13.7}_{-0.3}$	$3.5^{+0.9}_{-0.8}$	1.41/132	40.3
DISKIR obs 2	$2.45^{+0.06}_{-0.22}$	0.13 ± 0.01	1.61 ± 0.02	$80.3^{+18.9}_{-0.2}$	$1.59^{+0.08}_{-0.07}$	1.45/144	40.6
X-ray Only							
SIRF obs 1	2.35 ± 0.07	$2.1^{+0.3}_{-0.2}$	...	0.49 ± 0.07	...	1.27/131	40.3
SIRF obs 2	$2.8^{+0.2}_{-0.1}$	$1.25^{+0.07}_{-0.06}$	...	0.66 ± 0.03	...	1.19/143	40.6
MCD+COMPTT obs 1	$1.4^{+0.8}_{-0.4}$	$0.22^{+0.07}_{-0.05}$	7^{+1}_{-5}	<26.4	$2.9^{+0.9}_{-0.6}$	1.23/129	40.2
MCD+COMPTT obs 2	$1.6^{+0.2}_{-0.3}$	0.7 ± 0.2	12^{+6}_{-5}	$4.6^{+10}_{-3.5}$	1.7 ± 0.2	1.21/141	40.4

Note. Errors are limits indicating the 1σ confidence regions. Columns: (1) X-ray model, as described in Section 3.1. (2) Intrinsic hydrogen column density. (3) Inner disk temperature. (4) Photon index for the DISKIR model and the optical depth of the Comptonizing component for the MCD+CompTT model. (5) Inner disk radius for the accretion disk. For the DISKIR and MCD+COMPTT models these were calculated using the normalization. For the SIRF model they were estimated using the "spherization radius" (see Abolmasov et al. 2009) and the luminosity. See Section 3.1 for more details. (6) Electron temperature. (7) Reduced χ^2 values for the fit and the number of degrees of freedom. (8) Unabsorbed (intrinsic) luminosities between 0.3 and 10 keV.

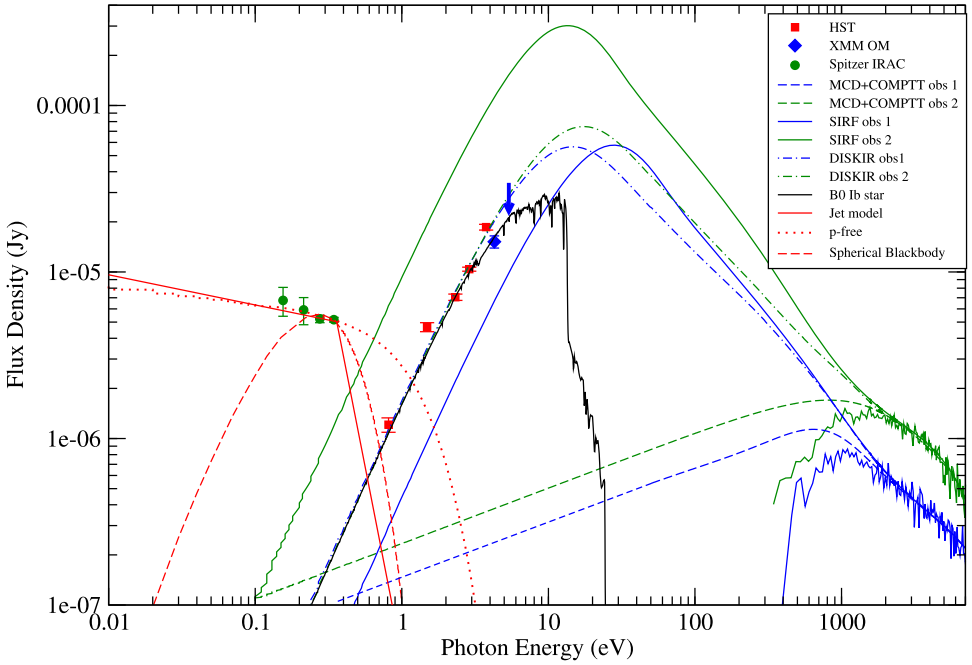

Figure 2. SED constructed in Section 3. The *HST* data are taken from Grisé et al. (2011), the *XMM* OM UV data from Berghea & Dudik (2012). The two representative X-ray data sets (*XMM-Newton* data sets 0112521101 and 0693851701 shown as obs 1 in blue and obs 2 in green, respectively) are taken from Luangtip et al. (2016). Error bars are 1σ.

mechanisms. We note that some fraction of the IR emission will also result from contamination from the bubble nebula. Grisé et al. (2011) found some red excess in the *I* band based on the stellar model fits to the *HST* data. However, the *HST* images from this study suggest that the *I*-band emission is not coming from nebular contamination, especially in the central location (Grisé et al. 2011). In addition, the *H* band fits the stellar continuum very well and does not show a similar excess. We explore the three remaining options for the excess below.

Heated Dust Shell: Emission from a heated dust shell is one explanation for the IR excess seen in Ho IX X-1. Rahoui et al. (2010) found evidence for a dust component with temperature ~400 K from the Galactic X-ray binary GRS 1915+105. GRS 1915+105 is a microquasar that has a red giant as a donor (Greiner et al. 2001). Rahoui et al. (2010) suggest that the dust component could be related to the dusty shell often found surrounding red giants. We fit a spherical blackbody model to the Ho IX X-1 IRAC data. This blackbody, shown in Figure 2, gives a dust temperature of ~1100 K and a radius of ~1400 $R_\odot$. However, the fit is quite poor, the χ^2_ν being much greater than 2, thereby precluding error estimates for the parameters. The dust temperature is normal for dusty shells around red giants; however, if the companion star is a blue supergiant, as the optical *HST* data suggest, it is unlikely to be surrounded by

dust. In addition, this blackbody emission does not fit the 5.8 and 8.0 μm data well. We therefore rule out this option as a viable model for the infrared emission in the ULX.

Circumbinary Disk: An alternative explanation for a dust component is the circumbinary disk proposed by Perez & Blundell (2010), Rahoui et al. (2010), and Muno & Mauerhan (2006) to explain the IR emission in X-ray binaries (SS 433, GRS 1915+105, A0620−00, and XTE J1118+480). Here the circumbinary disk is distinct from the accretion disk described in Section 3 and is composed of material that may have been lost through the L2 point (e.g., SS 433; see Perez & Blundell 2010). If Ho IX X-1 is more like these X-ray binaries, we might expect to see such a circumbinary disk in the infrared. In this case the blackbody model that we fit to the infrared data would represent emission from the inner circumbinary disk, while the redder 5.8 and 8.0 μm excess is likely emanating from the outer portion of the circumbinary disk as lower-temperature blackbody emission. The four IRAC data points that compose the IR excess in Ho IX X-1 are not sufficient to fit a complicated circumbinary disk model (e.g., Akeson et al. 2007; Hillen et al. 2015); however, in its simplest form, the circumbinary disk model is very similar to an irradiated disk model, only the source of illumination in the former case is the accretion disk and the star. We therefore fit a very simple p-free disk model to the four IRAC points. As can be seen from Figure 2, the data are consistent with this simple p-free disk ($p = 0.64^{+0.09}_{-0.06}$), but the disk vastly overpredicts the H-band flux and the temperature for the fit is unconstrained ($T > 1680$ K). We conclude that if a circumbinary disk is responsible for the IRAC emission in this object, then the optical and/or IR emission must be variable.

Jet Emission: In the jet emission scenario we expect a broken power law with a break in the IR, and we attempted to fit the combined IRAC and *HST* data with such a model. Extinction $E(B-V)$ was fixed at 0.26 and the break energy at 0.35 eV (approximately at the 3.6 μm IRAC band; see Figure 2). For comparison the break is at 0.12 eV for Cygnus X-1 and 0.48 for GX 339-4 (Rahoui et al. 2011). Inspection of the fit clearly indicates that the *HST* H-band flux is prohibitively low for a reasonable power-law model. The emission in H band fits the stellar model so well that any additional contribution from a jet-dominated power law would either severely overpredict the observed emission or suggest a power-law slope that is unrealistically steep (Blandford & Königl 1979; Falcke & Biermann 1995). Indeed, the spectral index of the fit in Figure 2 is −4.3 in the optical/IR compared with typical indices of −0.4 to −1.0 (Blandford & Königl 1979; Falcke & Biermann 1995). We conclude from this that either (a) the IR emission from Ho IX X-1 is *not* jet dominated or (b) the radio ejecta are transient as is thought to be the case with Ho II X-1 (Cseh et al. 2014). The multi-epoch nature of the *HST* and IR data results in a degeneracy in the models that can only be broken by a series of radio monitoring activities designed to detect the jet emission when it is in its most luminous state.

Based on the analysis presented in the previous sections, the IR emission in Ho IX X-1 suggests that the system contains a circumbinary disk much like those detected in X-ray binaries (e.g., SS 433, GRS 1915+105, A0620−00, and XTE J1118 +480) or emission from a variable jet such as that seen with Ho II X-1 (e.g., Cseh et al. 2014). In the transient jet scenario, simultaneous IR and optical data might uncover a more reasonable power-law slope and H-band emission that is significantly higher than observed in the data set presented here. We also find that the IR data are not well fit by a single blackbody, such as that expected from a dusty shell. However, in this case the simultaneity of the data will not significantly improve the fit, since the single blackbody fits neither the optical data nor the longer-wavelength IR data as well. The degeneracy between the circumbinary disk and transient jet theory underscores the need for simultaneous observations when observing ULX structure and environments. In this case, very sensitive radio observations of Ho IX X-1 may solidify these findings and help detect or constrain the power-law break and slope needed to confirm jet activity. Indeed, such radio observations have recently been obtained using the VLA B-array and will be published in a follow-up study to this paper. However, as this study also indicates, deep radio *monitoring* observations with VLA are also critical to providing information about the IR excess in this source in the event that the jet (if one exists) is variable.

5. CONCLUSIONS

Using *Spitzer* IRAC observations of Ho IX X-1, we have constructed an SED of the ULX. Two contiguous IRAC observations of Ho IX X-1 were made. The data sets at 5.8 and 8.0 μm are at the sensitivity limit of the IRAC instrument; however, combining these measurements yields a statistically significant detection in both bands. The combined measurements coupled with detailed fits to previous optical/UV and X-ray data of Ho IX X-1 suggest that the IR excess in this object is due to either a circumbinary disk such as those seen in SS 433 and other standard X-ray binaries or a variable jet such as that seen in Ho II X-1 by Cseh et al. (2014). Future high-sensitivity radio monitoring observations would be needed to break the degeneracy between the two models and determine whether the IR excess seen in Ho IX X-1 results from either mechanism.

We thank the anonymous referee for the very helpful suggestions that have greatly improved this paper. The authors thank Luangtip et al. for providing the X-ray data presented here and for their useful discussions. We also thank Michel Hillen, Hans Van Winckel, and Rachel Akeson for the useful discussions concerning circumbinary disk models and their application to this data set. T.P.R. acknowledges financial support from STFC as part of the consolidated grant ST/L00075X/1. This work is based on observations obtained from multiple telescope facilities, including (1) *XMM-Newton*, an ESA science mission with instruments and contribution directly funded by ESA Member States and NASA; (2) the NASA/ESA *Hubble Space Telescope* and the Hubble Legacy Archive, which is a collaboration between the Space Telescope Science Institute (STScI/NASA), the Space Telescope European Coordinating Facility (ST-ECF/ESA), and the Canadian Data Centre (CADC/NRC/CSA); and finally, (3) the NASA *Spitzer Space Telescope*, which is managed by the Jet Propulsion Laboratory with data obtained from the Spitzer Heritage Archive, which is maintained by the Spitzer Science Center (SSC), located on the campus of the California Institute of Technology and part of NASA's Infrared Processing and Analysis Center (IPAC). The *Spitzer Space Telescope* is a NASA mission managed by the Jet Propulsion Laboratory. This Web site is maintained by the Spitzer Science Center,

located on the campus of the California Institute of Technology and part of NASA's Infrared Processing and Analysis Center.

REFERENCES

Abolmasov, P., Fabrika, S., Sholukhova, O., & Afanasiev, V. 2007, AstBu, 62, 36
Abolmasov, P., Karpov, S., & Kotani, T. 2009, PASJ, 61, 213
Abolmasov, P., & Moiseev, A. V. 2008, RMxAA, 44, 301
Akeson, R. L., Rice, W. K. M., Boden, A. F., et al. 2007, ApJ, 670, 1240
Bachetti, M., Harrison, F. A., Walton, D. J., et al. 2014, Natur, 514, 202
Berghea, C. T., & Dudik, R. P. 2012, ApJ, 751, 104
Berghea, C. T., Dudik, R. P., Weaver, K. A., & Kallman, T. R. 2010a, ApJ, 708, 354
Berghea, C. T., Dudik, R. P., Weaver, K. A., & Kallman, T. R. 2010b, ApJ, 708, 364
Berghea, C. T., Weaver, K. A., Colbert, E. J. M., & Roberts, T. P. 2008, ApJ, 687, 471
Blandford, R. D., & Königl, A. 1979, ApJ, 232, 34
Cardelli, J. A., Clayton, G. C., & Mathis, J. S. 1989, ApJ, 345, 245
Cseh, D., Kaaret, P., Corbel, S., et al. 2014, MNRAS, 439, L1
Fabbiano, G. 1988, ApJ, 325, 544
Fabrika, S., Ueda, Y., Vinokurov, A., Sholukhova, O., & Shidatsu, M. 2015, NatPh, 11, 551
Falcke, H., & Biermann, P. L. 1995, A&A, 293, 665
Farrell, S. A., Webb, N. A., Barret, D., Godet, O., & Rodrigues, J. M. 2009, Natur, 460, 73
Fender, R., & Belloni, T. 2004, ARA&A, 42, 317
Feng, H., & Soria, R. 2011, NewAR, 55, 166
Gerke, J. R., Kochanek, C. S., Prieto, J. L., Stanek, K. Z., & Macri, L. M. 2011, ApJ, 743, 176
Gierliński, M., Done, C., & Page, K. 2008, MNRAS, 388, 753
Gierliński, M., Done, C., & Page, K. 2009, MNRAS, 392, 1106
Gladstone, J. C., Roberts, T. P., & Done, C. 2009, MNRAS, 397, 1836
Greiner, J., Cuby, J. G., McCaughrean, M. J., Castro-Tirado, A. J., & Mennickent, R. E. 2001, A&A, 373, L37
Grisé, F., Kaaret, P., Corbel, S., et al. 2012, ApJ, 745, 123
Grisé, F., Kaaret, P., Pakull, M. W., & Motch, C. 2011, ApJ, 734, 23
Hillen, M., de Vries, B. L., Menu, J., et al. 2015, A&A, 578, A40
King, A. R. 2008, MNRAS, 385, L113
La Parola, V., Peres, G., Fabbiano, G., Kim, D. W., & Bocchino, F. 2001, ApJ, 556, 47
Liu, J.-F., Bregman, J. N., Bai, Y., Justham, S., & Crowther, P. 2013, Natur, 503, 500
Luangtip, W., Roberts, T. P., & Done, C. 2016, MNRAS, 460, 4417
Makovoz, D., & Marleau, F. R. 2005, PASP, 117, 1113
Middleton, M. J., Heil, L., Pintore, F., Walton, D. J., & Roberts, T. P. 2015, MNRAS, 447, 3243
Middleton, M. J., Miller-Jones, J. C. A., Markoff, S., et al. 2013, Natur, 493, 187
Miller, B. W., & Hodge, P. 1994, ApJ, 427, 656
Motch, C., Pakull, M. W., Soria, R., Grisé, F., & Pietrzyński, G. 2014, Natur, 514, 198
Muno, M. P., & Mauerhan, J. 2006, ApJL, 648, L135
Pakull, M. W., & Grisé, F. 2008, in AIP Conf. Proc. 1010, A Population Explosion: The Nature Evolution of X-ray Binaries in Diverse Environments, ed. R. Bandyopadhyay et al. (Melville, NY: AIP), 303
Pakull, M. W., & Mirioni, L. 2002, arXiv:astro-ph/0202488
Pakull, M. W., & Mirioni, L. 2003, in Revista Mexicana de Astronomia y Astrofisica Conf. Ser. 15, Winds, Bubbles, and Explosions, ed. S. J. Arthur & W. J. Henney (Mexico City: Universidad Nacional Autónonoma de México), 197
Perez, M. S., & Blundell, K. M. 2010, MNRAS, 408, 2
Poutanen, J., Lipunova, G., Fabrika, S., Butkevich, A. G., & Abolmasov, P. 2007, MNRAS, 377, 1187
Rahoui, F., Chaty, S., Rodriguez, J., et al. 2010, ApJ, 715, 1191
Rahoui, F., Lee, J. C., Heinz, S., et al. 2011, ApJ, 736, 63
Ramsey, C. J., Williams, R. M., Gruendl, R. A., et al. 2006, ApJ, 641, 241
Revnivtsev, M., Sunyaev, R., Gilfanov, M., & Churazov, E. 2002, A&A, 385, 904
Soria, R., & Kuncic, Z. 2008, in AIP Conf. Ser. 1053, Observational Evidence for Black Holes in the Universe, ed. S. K. Chakrabarti & A. S. Majumdar (Melville, NY: AIP), 103
Stobbart, A.-M., Roberts, T. P., & Wilms, J. 2006, MNRAS, 368, 397
Strohmayer, T. E., & Mushotzky, R. F. 2003, ApJL, 586, L61
Sutton, A. D., Done, C., & Roberts, T. P. 2014, MNRAS, 444, 2415
Sutton, A. D., Roberts, T. P., & Middleton, M. J. 2013, MNRAS, 435, 1758
Tao, L., Kaaret, P., Feng, H., & Grisé, F. 2012, ApJ, 750, 110
Vierdayanti, K., Done, C., Roberts, T. P., & Mineshige, S. 2010, MNRAS, 403, 1206
Walton, D. J., Harrison, F. A., Grefenstette, B. W., et al. 2014, ApJ, 793, 21
Webb, N., Cseh, D., Lenc, E., et al. 2012, Sci, 337, 554
Weng, S.-S., Zhang, S.-N., & Zhao, H.-H. 2014, ApJ, 780, 147